Monthly Notices
of the
ROYAL ASTRONOMICAL SOCIETY

MNRAS **470,** 2959–2971 (2017)
Advance Access publication 2017 June 7

doi:10.1093/mnras/stx1394

Galactic googly: the rotation–metallicity bias in the inner stellar halo of the Milky Way

Prajwal R. Kafle,[1]★ Sanjib Sharma,[2] Aaron S. G. Robotham,[1] Raj K. Pradhan,[3] Magda Guglielmo,[2] Luke J. M. Davies[1] and Simon P. Driver[1,4]

[1]*ICRAR, The University of Western Australia, 35 Stirling Highway, Crawley WA 6009, Australia*
[2]*SIfA, A28 School of Physics, The University of Sydney, Sydney NSW 2006, Australia*
[3]*Central Department of Physics, Tribhuvan University, Kathmandu, Kirtipur 44618, Nepal*
[4]*SUPA, School of Physics & Astronomy, University of St Andrews, North Haugh, St Andrews KY16 9SS, UK*

Accepted 2017 June 2. Received 2017 June 2; in original form 2017 March 7

ABSTRACT

The first and second moments of stellar velocities encode important information about the formation history of the Galactic halo. However, due to the lack of tangential motion and inaccurate distances of the halo stars, the velocity moments in the Galactic halo have largely remained 'known unknowns'. Fortunately, our off-centric position within the Galaxy allows us to estimate these moments in the galactocentric frame using the observed radial velocities of the stars alone. We use these velocities coupled with the hierarchical Bayesian scheme, which allows easy marginalization over the missing data (the proper motion, and uncertainty-free distance and line-of-sight velocity), to measure the velocity dispersions, orbital anisotropy (β) and streaming motion ($v_{\rm rot}$) of the halo main-sequence turn-off (MSTO) and K-giant (KG) stars in the inner stellar halo ($r \lesssim 15$ kpc). We study the metallicity bias in kinematics of the halo stars and observe that the comparatively metal-rich ([Fe/H] > -1.4) and the metal-poor ([Fe/H] ≤ -1.4) MSTO samples show a clear systematic difference in $v_{\rm rot} \sim 20{-}40\,{\rm km\,s^{-1}}$, depending on how restrictive the spatial cuts to cull the disc contamination are. The bias is also detected in KG samples but with less certainty. Both MSTO and KG populations suggest that the inner stellar halo of the Galaxy is radially biased i.e. $\sigma_{\rm r} > \sigma_\theta$ or σ_ϕ and $\beta \simeq 0.5$. The apparent metallicity contrariety in the rotation velocity among the halo sub-populations supports the co-existence of multiple populations in the galactic halo that may have formed through distinct formation scenarios, i.e. *in situ* versus accretion.

Key words: Galaxy: formation – Galaxy: general – Galaxy: halo – Galaxy: kinematics and dynamics.

1 INTRODUCTION

The first and second moments of velocities and the orbital anisotropy of stars are essential parameters for the dynamical studies of astrophysical systems at all scales, ranging from the dwarf spheroidals (Łokas 2009; Diakogiannis et al. 2017), the Galactic halo (Frenk & White 1980; Bekki & Chiba 2001; Sirko et al. 2004; Battaglia et al. 2005; Smith, Wyn Evans & An 2009b; Bond et al. 2010; Kafle et al. 2012, 2013; Das & Binney 2016), the Andromeda galaxy (Watkins, Evans & An 2010; Veljanoski et al. 2013), distant galaxies (Watkins et al. 2010; Deason et al. 2012), galaxy groups and clusters (Carlberg et al. 1997; Wojtak & Łokas 2010; Duarte & Mamon 2015) to dark matter haloes in cosmological simulations (Wojtak, Gottlöber & Klypin 2013). These moments are crucial in measuring the underlying mass of the system via Jeans analysis, tracer mass formalism, etc. (Evans et al. 2003; Watkins et al. 2010; Kafle et al. 2014), and are useful in determining the overall shape of the gravitational potential (An & Evans 2016; Lynden-Bell 2016) and flattening of the dark matter halo (Bowden, Evans & Williams 2016). However, until recently, due to the unavailability of tangential motion and accurate distances in the case of our own Milky Way (MW) stellar halo, the moments have largely remained unknown.

With the onset of large spectroscopic endeavours such as the Sloan Extension for Galactic Understanding and Exploration (SEGUE; Yanny et al. 2009), a sub-survey of the Sloan Digital Sky Survey (SDSS; York et al. 2000) focused on Galactic science, it

★ E-mail: prajwal.kafle@uwa.edu.au

is now[1] possible to quantify the spatio-kinematic properties of the Galactic halo beyond the solar neighbourhood in unprecedented detail. For example, equipped with the full phase-space coordinates of stars, i.e. position, distance, line-of-sight velocity and proper motion, Smith et al. (2009a) study SDSS sub-dwarf stars and similarly, Bond et al. (2010) study SDSS main-sequence stars within the solar neighbourhood and find that the velocity anisotropy of the local halo is radially biased ($\beta \simeq 0.68$). Note, the velocity anisotropy $\beta \in (-\infty, 1)$ is a commonly used parameter to describe the orbital structure of a halo, where $\beta < 0$, $\beta = 0$ and $\beta > 0$ mean tangentially biased, isotropic and radially biased, respectively. It is given by

$$\beta = 1 - \frac{\sigma_\theta^2 + \sigma_\phi^2}{2\sigma_{\rm r}^2}, \quad (1)$$

where $\sigma_{\rm r}$, σ_θ, σ_ϕ are a short-form notation for the radial ($\sigma_{v_{\rm r}} = \langle v_{\rm r}^2 \rangle$), angular ($\sigma_{v_\theta} = \langle v_\theta^2 \rangle$) and azimuthal ($\sigma_{v_\phi} = \langle v_\phi^2 \rangle$) galactocentric velocity dispersions, in a spherical polar coordinate system. The velocity anisotropy β is a highly asymmetric function around the isotropy. Hence, it is occasionally sensible to use a modified definition of the velocity anisotropy expressed as $\beta/(2-\beta)$. The modified velocity anisotropy is symmetric and $\in [-1, 1]$, where 0 signifies an isotropic, <0 means a tangentially biased, and >0 means a radially biased halo.

At large distances, the proper motions of the halo stars are either unreliable or generally unavailable, which hinders a direct measurement of their velocity dispersions. However, our off-centric location in the Galaxy means that the galactocentric radial (r) and heliocentric radial (s) directions are not the same. This difference is more significant in the inner halo, at a distance of $r \lesssim$ a couple of times of R_0, where R_0 is the distance of the Sun from the Galactic Centre. Hence, in the inner halo the observed line-of-sight velocities of the stars can be expressed in terms of all three orthogonal galactocentric velocities ($v_{\rm r}$, v_θ, v_ϕ), or in other words the line-of-sight velocities have some contribution from the tangential galactocentric velocities. Provided we have a model that well represents the distribution of the halo stars, we can fit a model marginalized over the unknown tangential motions to the available four-dimensional data (position vector and a line-of-sight velocity), and thus estimate the velocity moments of the system. In the absence of proper motion, the approach of estimating moments of the velocities has been extensively used to predict the kinematics of the MW halo. For example, Sirko et al. (2004), Kafle et al. (2012), Kafle et al. (2013), Kafle et al. (2014) and King et al. (2015) fit an ellipsoidal distribution of velocities and similarly, Deason, Belokurov & Evans (2011a) apply an alternative power-law model to derive the halo kinematics. Using the marginalisation scheme, Kafle et al. (2012, 2013) studied halo Blue Horizontal Branch stars (BHBs), Kafle et al. (2014) studied both BHBs and K-Giant stars (KGs), while King et al. (2015) analysed a mixed bag of BHB and F-type stars to cumulatively construct the velocity dispersion and anisotropy of the outer halo. Interestingly, Kafle et al. (2012) found that the velocity anisotropy parameter of the Galactic halo is non-monotonic and has a prominent dip at a galactocentric radius of $r \simeq 18$ kpc. In their studies, King et al. (2015) find that the value of β at $15 \lesssim R/\mathrm{kpc} \lesssim 25$ is more tangentially biased, which they attribute to the difference in the spatial resolutions of the data sets and adopt a marginalization technique. A varying level of undulations in the anisotropy parameter has also been observed in simulated haloes (Rashkov et al. 2013; Loebman et al. 2017). There are a number of proposed scenarios that could explain such a feature, e.g. a transition from inner to outer halo or a local shell-like structure at the given radius. Moreover, it can also be due to the unrelaxed stars dispersed from the kinematically coherent satellite galaxies that are aligned with kinematically coherent planar structures; assuming that such planar structures have strong rotation as suggested by Ibata et al. (2013), Pawlowski, McGaugh & Jerjen (2015), Libeskind et al. (2015) and Ibata et al. (2015), etc. Recently, Loebman et al. (2017) suggest that a major merger as early as redshift $z \sim 1$ can also result in a tangential dip in the value of β over a wide range of radii. While Bird & Flynn (2015) suggest that such a feature in the velocity anisotropy run of the halo is a transitory phase, Loebman et al. (2017) conclude that such dips are long-lived in the *in situ* stellar halo. In any case, there is currently no consensus view as to what causes such velocity anisotropy changes. Finally, in the outer halo there have been recent attempts to utilize multi-epoch *Hubble Space Telescope* data to estimate the halo velocity dispersion. In particular, recently Cunningham et al. (2016) used the Galactic foreground stars along the M31 galaxy and found that the halo is isotropic at $r/\mathrm{kpc} \sim 25$. In Fig. 10, we summarize the recent (this paper inclusive) measurements of the halo velocity anisotropy.

As mentioned earlier, we do not have a statistically robust sample of the halo stars yet with which to constrain a detailed halo kinematic map. This is largely due to the fact that they are difficult and inefficient to identify with current ground-based telescopes. This makes the attempt to construct a comprehensive model for the formation history of the galactic halo a challenging task. Observations suggest that the halo is partly formed *in situ* and partly by accretion, the so called dual origin of the halo (e.g. Majewski 1992; Carollo et al. 2007, 2010; Deason et al. 2011a; Beers et al. 2012; Kafle et al. 2013; Zuo et al. 2017, etc.), and are supported by the findings from recent cosmological hydrodynamical simulations of galaxy formation (Zolotov et al. 2009; Font et al. 2011; McCarthy et al. 2012; Tissera et al. 2014). The spatio-kinematics of the *in situ* component dominating the inner region of the halo are thought to resemble that of the disc flattening with net prograde rotation. The accreted component dominates the outer region of the halo and is found to have retrograde motion. The veracity of these claims, however, has been challenged and demonstrated not to be robust (Schönrich, Asplund & Casagrande 2011; Fermani & Schönrich 2013b). Schönrich et al. (2011) identify unphysical Gaussian analysis of the azimuthal velocity distribution, inaccurate distances of the main-sequence stars and a lack of proper treatment of uncertainties as the main limitations of the Carollo et al. (2007, 2010) and Beers et al. (2012) analysis; for the full account of this refer to Schönrich, Asplund & Casagrande (2014). A re-analysis of their data also fails to find any reliable evidence for a counter-rotating halo component, and hints that even if a distinct counter-rotating halo exists, the magnitude of the rotation must be comparatively much weaker than the earlier claims of 40–70 km s^{-1} (Carollo et al. 2007, 2010). Furthermore, in the light of improved galactic models and increasing evidence of lighter Galaxy halo mass (e.g. Xue et al. 2008; Gibbons, Belokurov & Evans 2014; Kafle et al. 2014; Eadie & Harris 2016, etc.), the impact of the model of the Galactic potential assumed in Carollo et al. (2007, 2010) has not been explored. A star in a lighter Galactic halo will attain higher maximum distance above and below the Galactic plane as compared to a heavier halo. This will change the classification of stars into an inner and an outer halo

[1] For an overall summary of the earlier works such as Frenk & White (1980), Ratnatunga & Freeman (1989), Sommer-Larsen, Flynn & Christensen (1994), etc., we refer the reader to the review articles Majewski (1993), Helmi (2008) and Bland-Hawthorn & Gerhard (2016) that already cover the topic extensively.

component. Adding to the confusion, Kafle et al. (2013) find that the SEGUE BHBs do not show any radial segregation into inner prograde and outer retrograde halo. Instead, they observe a distinct dichotomy in the kinematics among the comparatively metal-rich ([Fe/H] > -2) and metal-poor ([Fe/H] ≤ -2) BHB sub-samples, even with the new distance calibration by Fermani & Schönrich (2013a). Hattori et al. (2013) report a similar metallicity bias in the inner-halo kinematics whereas Fermani & Schönrich (2013b) claim that after flagging out ∼500 metal-poor stars from the original BHB catalogue of Xue et al. (2011) the apparent discrepancy in the rotation signal detected in the above work diminishes. Moreover, Fermani & Schönrich (2013b) confirm that the conclusion of a non-rotating halo holds when they utilize proper motions of stars with both a model dependent and a direct approach using de-projected line-of-sight velocities.

To further investigate the issue of halo duality, we require a large number of halo stars with reliable proper motions and robust distance estimates. In addition, it would also be informative to have halo stars from different types of stellar populations with different ages and metallicity. In the near future, *Gaia* (Brown, Velázquez & Aguilar 2005) will provide parallaxes and proper motions as well as radial velocities for a large number of halo stars in the solar neighbourhood, and this will allow us to study the kinematics of the halo in greater detail. Similarly, chemical footprints of halo stars provided by surveys such as GALactic Archaeology with HERMES (GALAH; De Silva et al. 2015; Martell et al. 2017) will also open a completely new dimension to further test the theory. For now, we focus on studying the kinematics of the halo KGs and halo main-sequence turn-off stars (MSTOs) using data provided by the SEGUE survey.

The rest of this paper is organized as follows. Section 2 describes our stellar halo samples. Section 3 provides the formulary for the kinematic measurement and tests on synthetic data are provided in Section 4. In Section 5, we present and discuss our results. Finally, we summarize our findings in Section 6.

2 DATA

2.1 Main-sequence turn-off stars

We construct an MSTO data set by querying SDSS DR13 (SDSS Collaboration et al. 2016) with the following colour and magnitude limits:

$$\begin{cases} 0.15 < g_0 - r_0 < 0.4 \\ 3.5 < \log g < 4.7 \\ 14 < r_0 < 20 \end{cases}, \tag{2}$$

where g_0 and r_0 are the extinction corrected magnitudes and g denotes the surface gravity. The above colour restriction is similar to the one used in Bell et al. (2010) and Sharma et al. (2011a). For each star in our initial sample, we calculate an absolute magnitude ($M_{\rm r}$) using the following formula (Ivezić et al. 2008):

$$\begin{aligned} \delta M_{\rm r} &= 4.5 - 1.11[{\rm Fe/H}] - 0.18[{\rm Fe/H}]^2, \\ M_{\rm r} &= -5.06 + 14.32(g_0 - i_0) - 12.97(g_0 - i_0)^2 \\ &\quad + 6.127(g_0 - i_0)^3 - 1.267(g_0 - i_0)^4 \\ &\quad + 0.0967(g_0 - i_0)^5 + \delta M_{\rm r}. \end{aligned} \tag{3}$$

We expect some spread $\sigma_{M_{\rm r}}$ around $M_{\rm r}$, which we predict to increase as we go redward in $g_0 - i_0$ colour and also as we go lower in [Fe/H].

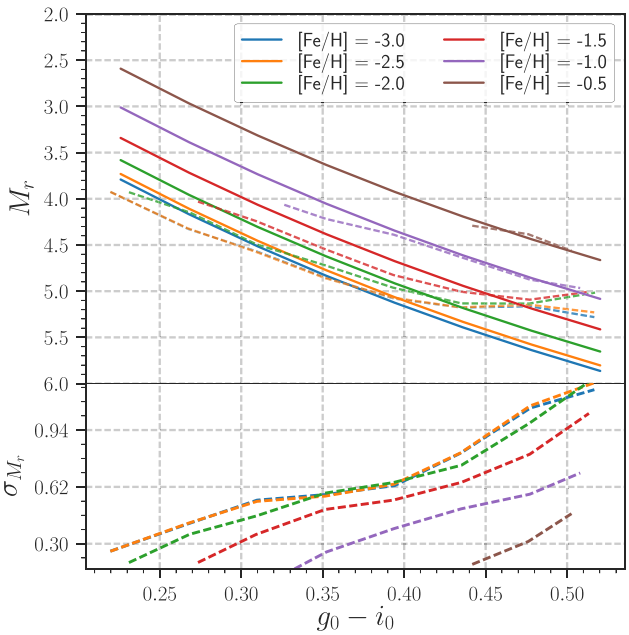

Figure 1. Absolute magnitude–colour relation for MSTOs. The solid and dashed lines in the top panel show r-band absolute magnitude, $g_0 - i_0$ colour and metallicity [Fe/H] relation obtained from Ivezić et al. (2008) and Sharma et al. (2011b, GALAXIA), respectively. Bottom panel shows dispersion in the r-band absolute magnitude as a function of $g_0 - i_0$ colour derived using MSTOs generated from the GALAXIA.

To quantify this relation, we generate a synthetic catalogue of stars using GALAXIA[2] (Sharma et al. 2011b) from which we select MSTOs using the same selection function as above. The dispersion in $\sigma_{M_{\rm r}}$ as a function of the $g_0 - i_0$ and [Fe/H] predicted by GALAXIA is shown in the bottom panel of Fig. 1. We interpolate $\sigma_{M_{\rm r}}(g_0 - i_0, [{\rm Fe/H}])$ relation shown above and then use it to compute the corresponding value of $\sigma_{M_{\rm r}}$ for SEGUE MSTOs given a $g_0 - i_0$ colour and [Fe/H].

Likewise, using GALAXIA we can also derive a $M_{\rm r}(g_0 - i_0, [{\rm Fe/H}])$ relation, which is shown with the dashed lines in the top panel of Fig. 1. But since the relation given in equation (3) is known to be robust for SDSS stars (Ivezić et al. 2008) we decide not to use the $M_{\rm r}$ predicted by GALAXIA in our final results. However, refer to Section 4 for a comparison between distances estimated assuming two definitions of $M_{\rm r}$ given above, and also refer to Section 5.2 to understand the impact of this choice.

In the top panel of Fig. 1, solid lines demonstrate the colour and metallicity dependence of $M_{\rm r}$ given by equation (3). With the estimated $M_{\rm r}$ and associated dispersion $\sigma_{M_{\rm r}}$, we calculate the distances to the MSTOs using the photometric parallax relation given by

$$s/{\rm kpc} = 10^{\mu/5-2}, \tag{4}$$

[2] GALAXIA is a population synthesis software for creating a synthetic survey of the MW based on its embedded model. GALAXIA uses isochrones from the Padova data base to compute photometric magnitudes for the model stars (Bertelli et al. 1994; Marigo et al. 2008, but see Girardi et al. (2004) for SDSS-specific details). The web-link to the GALAXIA software is http://galaxia.sourceforge.net/ and for the full documentation visit the web-link http://galaxia.sourceforge.net/Galaxia3pub.html.

where $\mu = r_0 - M_r$ is the distance modulus. For an uncertainty of σ_{r_0} in the apparent magnitude (r_0) and δM_r in the absolute magnitude (M_r), we calculate the uncertainty in the distance modulus σ_μ using,

$$\sigma_\mu = \sqrt{\sigma^2_{M_r} + \sigma^2_{r_0}}. \quad (5)$$

This leads to a typical uncertainty of roughly 25 per cent in the estimated distances. Note, when we use equation (4) to convert distance modulus μ to distance s, a Gaussian error function assumed for μ does not translate to a Gaussian error function for the distance. Hence, in Section 3 while measuring the kinematics we prefer to work in distance modulus space instead of distance.

Importantly, to ensure high fidelity we further impose quality cuts to only keep stars with *elodiervfinalerr* > 0, *seguePrimary* $= 1$ and $zwarning = 0$ or 16 (taken from the SEGUE catalogue). The SEGUE Stellar Parameter Pipeline (SSPP, Lee et al. 2008; Smolinski et al. 2011) requires a signal-to-noise ratio (S/N) of at least 10 to estimate spectroscopic parameters, and the estimates tend to improve for higher S/N. We hope that the quality (or lack thereof) of spectra reflects on the uncertainties quoted in the spectroscopic parameters that we consider in our kinematic measurements (Section 3). However, to avoid edge cases we only use stars with S/N > 15. Also, to select the potential halo stars we only use stars with the height above the galactic plane $|z|$ larger than 4 kpc as we wish to cull the disc contaminants. Our ability to measure tangential velocity dispersions from $v_{\rm los}$ diminishes at larger radii (Hattori et al. 2017). Moreover, we observe that uncertainties in distances increases at large radii. Therefore, in this paper we confine our study to the galactocentric radius of $r/\mathrm{kpc} < 15$.

Note, as recommended in the SEGUE documentation, we use *elodiervfinal* for radial velocities, *elodiervfinalerr* for uncertainties in radial velocities and *fehadop* for the [Fe/H] metallicity. In our final sample, 90 per cent of stars have <20 per cent uncertainty in radial velocity.

2.2 K-giant stars

We directly obtain KGs from the publicly available catalogue of Xue et al. (2014), which is also constructed from the SEGUE project. These stars are selected based on $g_0 - r_0$ and $u_0 - g_0$ colours, and gravity. The distance to the stars are calculated using the photometric parallax relation for which they obtain an absolute magnitude by matching to a set of observables, i.e. colour, apparent magnitude and metallicity of a star to the metallicity-dependent colour–absolute magnitude relations obtained from clusters. Typical uncertainty in the measured distance is claimed to be 16 per cent. Finally, to make this selection comparable to our MSTO sample, we impose $|z|/\mathrm{kpc} > 4$ cut. Compared to the MSTOs, KGs have better distance measurements, hence we relax the radial criteria and analyse KGs within $r/\mathrm{kpc} < 17$. This helps to increase the KG sample size and allows us to determine comparatively more robust kinematics when using different metallicity ranges.

Finally, in Fig. 2(a) we show sky coverage of our selected MSTO and KG samples in galactic longitude (l) and latitude (b). Similarly, in Fig. 2(b) we present the number distribution of our stellar samples as a function of galactocentric radius r for different metallicity ranges as labelled in the figure. The metallicity division for both the MSTO and KG samples is defined at the median [Fe/H] of the full sample. We test that a shift of 0.2 dex to the division in either direction does not change our conclusions. In the figure, the comparatively metal-rich ([Fe/H] > -1.4) and the metal-poor ([Fe/H] ≤ -1.4) MSTOs/KGs are shown in blue and red colours, respectively, where the solid line represents the MSTOs and the dashed line represents the KGs. As labelled in the figure, the number of MSTOs with [Fe/H] > -1.4, MSTOs with [Fe/H] ≤ -1.4, KGs with [Fe/H] > -1.4 and KGs with [Fe/H] ≤ -1.4 are 6693, 7426, 513 and 968, respectively. We find that the metal-rich and the metal-poor MSTOs or KGs have roughly similar radial distributions. Additionally, in panels (c) and (d) we show spatial distributions of our final MSTO (black dots) and KG (green dots) samples. The dashed blue lines in panel (c) shows $|z| = 4$ kpc demarcation; the spatial limit applied to cull disc stars. The radial spikes seen in panel (c) and (d) are the natural feature of the pencil-beam observation made by the SEGUE survey.

3 METHOD

From our heliocentric vantage point in the MW we can observe the angular positions in the sky (i.e. Galactic longitude l and latitude b), distance (s), line-of-sight velocity ($v_{\rm los}$) and proper motion (tangential motion in the sky μ_l and μ_b) for each star, albeit with some uncertainty. Given the distance of the Sun (R_0) from the Galactic Centre, its relative motion with respect to the Local Standard of Rest (LSR) of the Galaxy ($U_\odot$, $V_\odot$, $W_\odot$) and the motion of the LSR with respect to the Galactic Centre ($v_{\rm LSR}$), we can convert the heliocentric coordinates to the Galactocentric reference frame according to the Appendix. The velocity distribution of halo stars in the Galactocentric reference frame can then be described by a multivariate Gaussian model of the form:

$$p(v_r, v_\theta, v_\phi|\Theta, l, b, s(\mu)) \propto \mathcal{N}(v_r|0, \sigma_r)\mathcal{N}(v_\theta|0, \sigma_\theta) \mathcal{N}(v_\phi|v_{\rm rot}, \sigma_\phi), \quad (6)$$

where $\mathcal{N}(.|\mathrm{mean, variance})$ refers to a Normal distribution, and $\Theta = \{\sigma_r, \sigma_\theta, \sigma_\phi, v_{\rm rot}\}$ represents a set of parameters that include the mean azimuthal velocity ($v_{\rm rot} = \langle v_\phi \rangle$) and the velocity dispersion profiles in spherical coordinates along the radial (r), angular (θ) and azimuthal (ϕ) directions. Note, here a positive value for $v_{\rm rot}$ means retrograde motion whereas a negative value means prograde motion i.e. rotating in the same direction the Galactic disc rotates. Following the recent works of Smith et al. (2009b), Bond et al. (2010), King et al. (2015) and Das & Binney (2016) we assume that the velocity ellipsoids of the halo stars are aligned along the coordinate frame directions of the spherical polar coordinate centred at the Galactic Centre. As a consequence, the covariance matrix of the velocity ellipsoid is assumed to be diagonal, i.e. we ignore correlations among radial, angular and azimuthal velocities. In general, tangential velocities (v_l and v_b or proportionally proper motion) of the stellar halo stars are either completely unknown or not known accurately. But, the distance modulus and line-of-sight velocities are known with uncertainties of σ_μ and $\sigma_{v_{\rm los}}$, respectively. The true uncertainty-free version of the distance modulus μ' and line-of-sight velocity $v'_{\rm los}$ are not accessible and we treat these as hidden/latent variables. We marginalize over the unknowns – tangential velocities, true distance modulus and true line-of-sight velocities – to obtain

$$p(v_{\rm los}|\Theta, l, b, \mu, \sigma_\mu, \sigma_{los}) = \int\int\int\int p(v_l, v_b, v_{\rm los}|\Theta, l, b, \mu', v'_{\rm los}) \; p(v'_{\rm los}|v_{\rm los}, \sigma_{v_{\rm los}}) \; p(\mu'|\mu, \sigma_\mu) \; p(\mu') \; \mathrm{d}v_l \; \mathrm{d}v_b \; \mathrm{d}v'_{\rm los} \; \mathrm{d}\mu'. \quad (7)$$

To determine the distance modulus distribution $p(\mu)$ we assume that $p(\mu)\,\mathrm{d}\mu = \rho(l, b, s)4\pi s^2 \mathrm{d}s$ and utilize equation (4) to derive

$$p(\mu) \propto s(\mu)^3 \rho(l, b, s(\mu)). \quad (8)$$

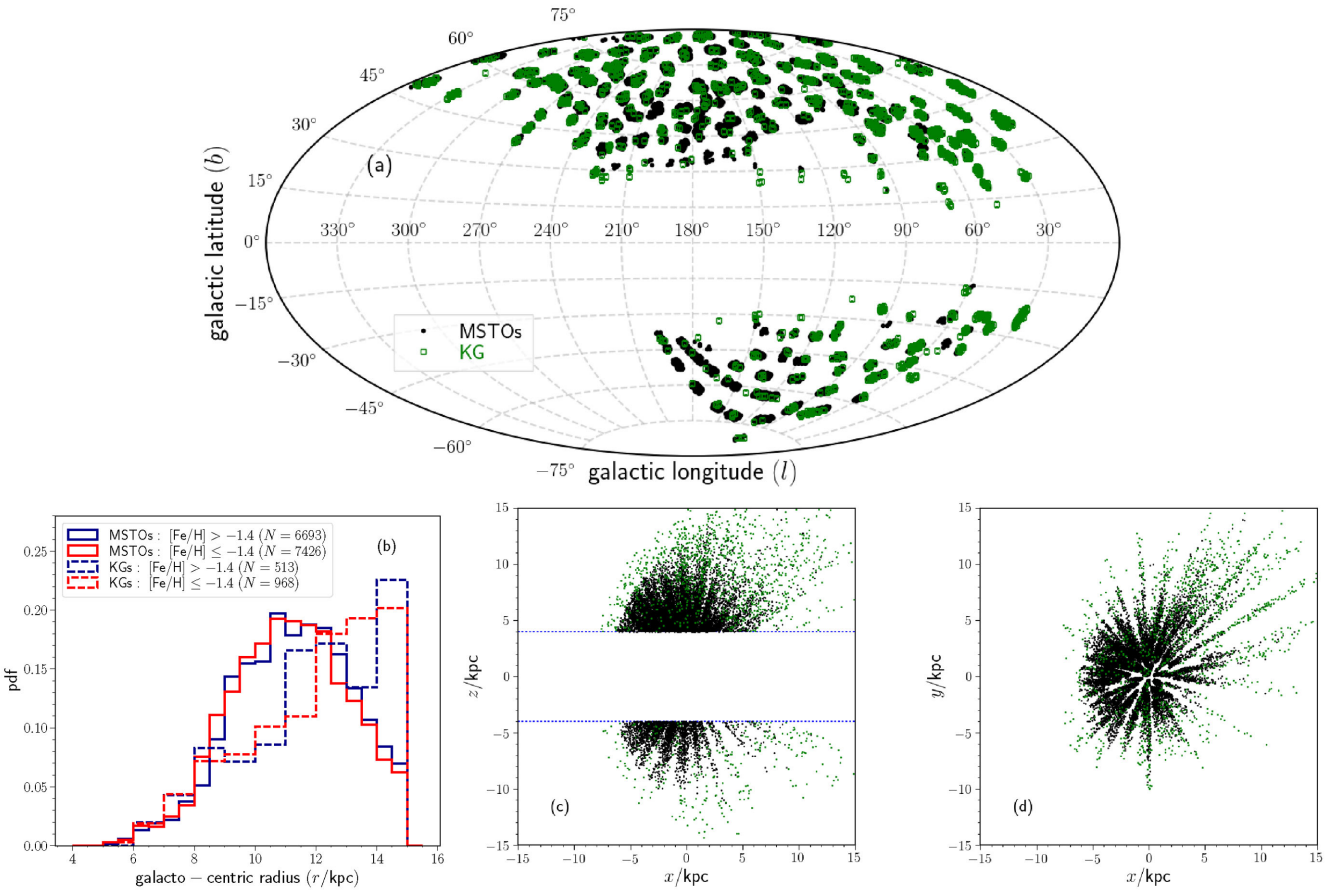

Figure 2. Data properties of the SEGUE MSTO and KG stars. Panel (a) shows sky coverage of the stars used in this work in the galactic coordinates (l, b), panel (b) shows the number distribution of the stars in the stellar sub-samples in different [Fe/H] ranges and panels (c) and (d) show projection in Cartesian coordinates. The blue dashed lines in panel (c) denotes $|z| = 4$ kpc restriction we adopt to cull disc stars.

Here, $\rho(l, b, s(\mu))$ is a galactocentric radial distribution of the halo stars. Fortunately, from recent observational evidence such as Bell et al. (2008), Watkins et al. (2009), Sesar, Jurić & Ivezić (2011), Deason, Belokurov & Evans (2011b), Akhter et al. (2012), and Xue et al. (2015) it is known that the logarithmic density distribution of the smooth component of the inner stellar halo follow, a power law given by $\rho \propto r(l, b, s(\mu), R_0)^{-\alpha}$ with a power-law slope $\alpha \simeq 2.5$. However, in Section 5 we investigate the effect of our choice of power-law slope on our final results.

Finally, given the data $\mathrm{D} = \{l, b, \mu \pm \sigma_\mu, v_{\rm los} \pm \sigma_{v_{\rm los}}\}$ of N stars we estimate Θ by

$$p(\Theta|D) \propto p(\Theta) \prod_i^N p(v_{\rm los}|\Theta, l, b, s, \sigma_s, \sigma_{\rm los}), \quad (9)$$

where $p(\Theta)$ represents the priors on model parameters Θ. Equation (7) does not have an analytical form. Hence, marginalization needs to be done numerically using some deterministic integration techniques, which are inefficient. Alternatively, we can treat the missing data or unknowns, v_l, v_b, s' and $v'_{\rm los}$, as latent variables by setting them up as a Hierarchical Bayesian model and estimating them simultaneously alongside Θ using the Metropolis-within-Gibbs algorithm (Sharma et al. 2014, 2017)[3]. To ensure the stability of the distributions of parameters around certain values, we run the algorithm for a sufficient autocorrelation time. We consider the values corresponding to the median of the posterior distributions of the parameters Θ as the best estimates, and the 16th and 84th percentiles of the distributions as its associated uncertainties.

We choose flat priors for $(\sigma_{\rm r}, \sigma_\theta, \sigma_\phi)/\,{\rm km\,s^{-1}} \in [10, 250]$, $v_{\rm rot}/\,{\rm km\,s^{-1}} \in [-60, 60]$ and $(v_l, v_b)/\,{\rm km\,s^{-1}} \in [-600, 600]$. We assume $R_0 = 8.2$ kpc (Bland-Hawthorn & Gerhard 2016), $U_\odot = 11.1\,{\rm km\,s^{-1}}$, $V_\odot = 12.24\,{\rm km\,s^{-1}}$, $W_\odot = 7.25\,{\rm km\,s^{-1}}$ (Schönrich, Binney & Dehnen 2010) and $v_{\rm LSR} = 236.2\,{\rm km\,s^{-1}}$ (Reid & Brunthaler 2004). However, later in the text we investigate and discuss the implications of our choice of priors on our final results.

Finally, we would like to highlight that our method also has an immediate application for the upcoming data releases of *Gaia* even if it could not provide a reliable radial velocity for halo stars. In such a case we can marginalize over $v_{\rm los}$ and utilize the observed parallax distances, proper motion and associated uncertainties instead.

4 TESTS WITH SIMULATED DATA SETS

There are two important aspects of our analysis that need to be tested. First, the efficacy of our marginalization technique (equation 7) and second, the effect of observational biases and variance in our final results.

For the first aspect we perform a simple test, where we construct a set of synthetic data that mimic spatial distributions of

[3] The software is available at https://github.com/sanjibs/bmcmc.

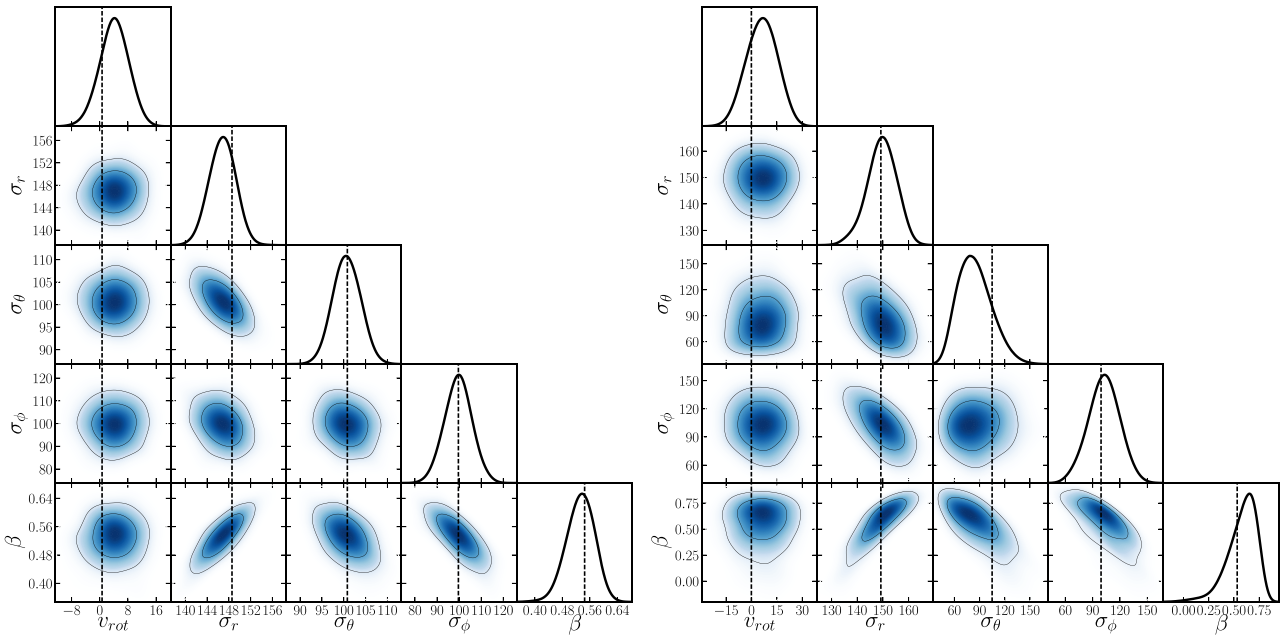

Figure 3. Results of the test runs on the metal-poor samples of MSTOs (left-hand panel) and KGs (right-hand panel) with radially biased synthetic velocity distributions. The contours show joint posterior probability distributions of the velocity moments for the synthetic data and the histograms show one-dimensional marginalized posterior distribution. The synthetic data has the same number of stars and sky footprint as the SEGUE data, in fact it uses exactly the same values of l, b, μ and $\sigma_{v_{\rm los}}$ as the SEGUE data. Dashed vertical lines show the true values of the velocity moments of the synthetic data. The contours depict 1σ and 2σ credibility intervals.

our MSTO/KG sample. Here we adopt the original position vector (l, b, $\mu \pm \sigma_\mu$) of the SEGUE MSTOs/KGs sample. This way we preserve the effect of the survey footprint and sample size in the test analysis identical to our final analysis. We then sample equation (6) to obtain synthetic velocities, that we project to the observational space and replace the observed SEGUE line-of-sight velocity, $v_{\rm los}$, with the synthetic $v_{\rm los}$. To realize the error distribution of $v_{\rm los}$ we pair the sampled, $v_{\rm los}$, with the actual, $\sigma_{\rm los}$, of the SEGUE stars. Later we analyse the observed data in an identical manner. First, in the left-hand panel of Fig. 3, we show a case of the SEGUE MSTO sample with radial velocity anisotropy. The contours in the figure show the 1σ and 2σ regions of the joint posterior probability distributions of the model parameters, as well as the derived velocity anisotropy β, sampled from the Markov chain Monte Carlo (MCMC) runs. The input value of each parameter in this example were $\sigma_{\rm r} = 150$ km s^{-1}, $\sigma_\theta = \sigma_\phi = 100$ km s^{-1} and $v_{\rm rot} = 0$ km s^{-1}, which could be slightly altered while subsampling due to the stochastic nature of the randomness trials. The true values are shown with the vertical dashed lines in the figure. Similarly, in the right-hand panel of Fig. 3 we also show a case of the SEGUE KG sample, with the same values for the model parameters as for the MSTO case. We observe that the intrinsic velocity moments in both the above mentioned cases are recovered within the 1σ credibility interval. We also repeat the exercise with possible alternative scenarios, for example assuming isotropic/tangential velocity anisotropies for MSTOs/KGs and also for positive and negative values for $v_{\rm rot}$. Furthermore, we also repeat the above set of tests with metal-rich subsets of MSTOs/KGs. In all of these additional cases we achieve similar levels of accuracy as demonstrated in Fig. 3.

Now for the second part we perform a more realistic test, for which we invoke GALAXIA. Here we aim to understand the effects of observational errors, mainly due to sample selection, survey footprint, distance estimations and random errors in the observables, on the final kinematics. For this we first generate synthetic MSTO stars using GALAXIA with a more relaxed selection criteria (to allow margin for uncertainties in each parameter) for r_0 and $g_0 - r_0$ than the one provided in equation (2). Then we jitter the colour ($g_0 - r_0$), and also the surface gravity ($\log g$) and the metallicity ([Fe/H]) for each star assuming Gaussian error distributions with dispersions equal to 0.03 mag, 0.28 dex and 0.20 dex, respectively.[4] Now, we impose exact selection criteria provided in equation (2) on the synthetic catalogue. Furthermore, to mimic SEGUE footprint shown in Fig. 2(a) we employ HEALPIX (with npixel = 768; Gorski et al. 1999; Górski et al. 2005) and only select stars in the pixels that overlap with the SEGUE footprint. Next, we use the Ivezić et al. (2008) relation given in equation (3) to derive $M_{\rm r}$ for the synthetic MSTO as we did for the SEGUE MSTOs in Section 2. We find that $M_{\rm r}$ derived from GALAXIA is systematically higher by an average $+0.37$ mag compared to the Ivezić et al. (2008) relation. This could be due to zero-point offsets in SDSS magnitudes provided in the isochrones. Similarly, we calculate dispersion from the interpolated function $\sigma_{M_{\rm r}}(g_0 - i_0, {\rm [Fe/H]})$ derived in Section 2. Then we use equation (4) to calculate distances to the synthetic MSTOs. In Fig. 4, we compare the estimated distances for the synthetic MSTOs against their intrinsic distances provided by GALAXIA. The blue dashed line in the figure shows 1:1 correspondence between the two distances whereas the colour code in the figure represents the number of stars in each pixel. We can see that the two distances are in reasonable agreement, considering the systematic as well as the realistic (observational-like) errors. To avoid confusion, we would like to re-emphasize here that the Ivezić et al. (2008)

[4] We adopt uncertainties in stellar and photometric parameters of the SEGUE stars from http://www.sdss3.org/dr9/spectro/sspp_internal.php.

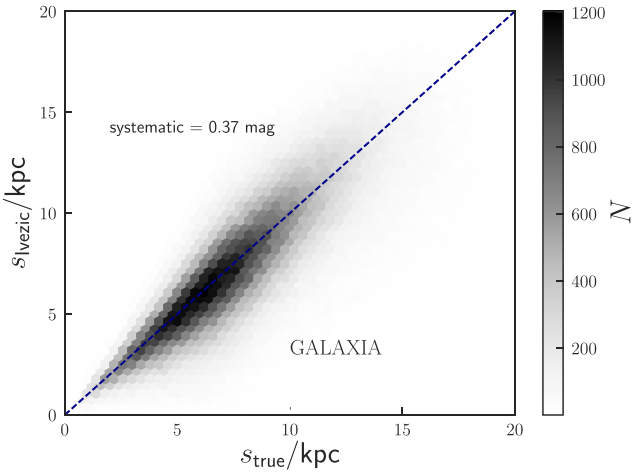

Figure 4. A comparison between distances estimated using Ivezić et al. (2008) relation and intrinsic distances for synthetic MSTO sample obtained from GALAXIA.

relation can be assumed to be robust for the SDSS/SEGUE stars, hence needs no such correction. Rather, to mock SEGUE stars, $M_{\rm r}$ of the GALAXIA MSTOs need to be corrected by $+0.37$ mag. Utilizing the estimated distances and angular positions we derive the galactocentric position vector of the tracers. Then we impose spatial cuts of $r < 15$ kpc and $|z| < 4$ kpc to select the halo stars, as we do in the case of the SEGUE MSTOs. In the end, we also add a Gaussian random error to the radial velocities of the synthetic MSTOs, where the error distribution is kept the same as the error distribution of the radial velocities of the observed data (SEGUE MSTOs). Finally, we feed processed synthetic MSTO data $\mathrm{D} = \{l, b, \mu \pm \sigma_\mu, v_{\rm los} \pm \sigma_{v_{\rm los}}\}$ to our machinery (Section 3) to derive the model parameters. Joint probabilities of the model parameters obtained from this exercise are shown in Fig. 5. Dashed vertical lines at $\sigma_{\rm r} = 134.9$ km s^{-1}, $\sigma_\theta = 84.8$ km s^{-1}, $\sigma_\phi = 84.6$ km s^{-1} and $v_{\rm rot} = -0.3$ km s^{-1} show the intrinsic values of the velocity moments of the synthetic MSTOs. We can see that the true values of the moments fall within 1σ regions of the estimated kinematics. The above tests demonstrate that in the radial range of our data $r \in [0, 15]$ kpc, $v_{\rm los}$ information is sufficient to recover the full kinematics ($\sigma_{\rm r}$, σ_θ, σ_ϕ, $v_{\rm rot}$) of the halo, even when the observational biases/variances are taken into account.

5 RESULTS

5.1 Kinematics of the turn-off and K-giant stars

Now, we apply our scheme to the SEGUE MSTO and KG star catalogues constructed in Section 2. The joint posterior probability distributions of the model parameters ($\sigma_{\rm r}$, σ_θ, σ_ϕ, $v_{\rm rot}$) and derived velocity anisotropy (β) obtained using the MCMC simulation for the MSTOs and KGs are shown in Figs 6 and 7, respectively. The two red contours show 1σ and 2σ credibility intervals for a metal-poor ([Fe/H] ≤ -1.4) sub-sample. Likewise, the blue contours show the distributions for a comparatively metal-rich ([Fe/H] > -1.4) sub-sample. As already mentioned previously, we restrict our analysis to r/kpc $\lesssim 15$ for MSTOs and to r/kpc $\lesssim 17$ for KGs.

The most striking feature in the case of MSTOs (Fig. 6) is that there is a clear metallicity dependence in the estimated velocity moments. We find that the metal-rich and metal-poor samples have opposite mean azimuthal velocity ($v_{\rm rot}$), meaning the metal-rich

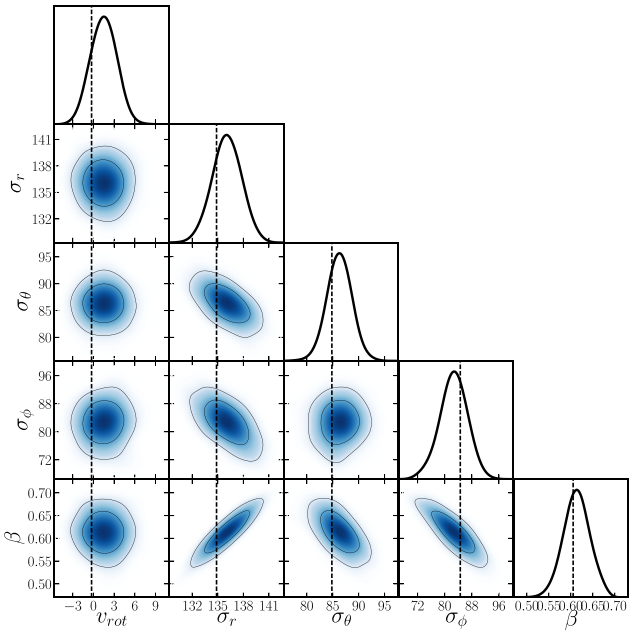

Figure 5. Results of the test runs on the synthetic MSTOs sampled from GALAXIA and convolved with SEGUE-like error functions. The contours show joint posterior probability distributions of the velocity moments for the synthetic data and the histograms show one-dimensional marginalized posterior distribution. The synthetic data has the same number of stars and roughly the same sky footprint as the SEGUE data. Moreover, they are convolved with SEGUE-like uncertainties in photometry, stellar parameters and radial velocity. Dashed vertical lines show the true values of the velocity moments of the synthetic data. The contours depict 1σ and 2σ credibility intervals.

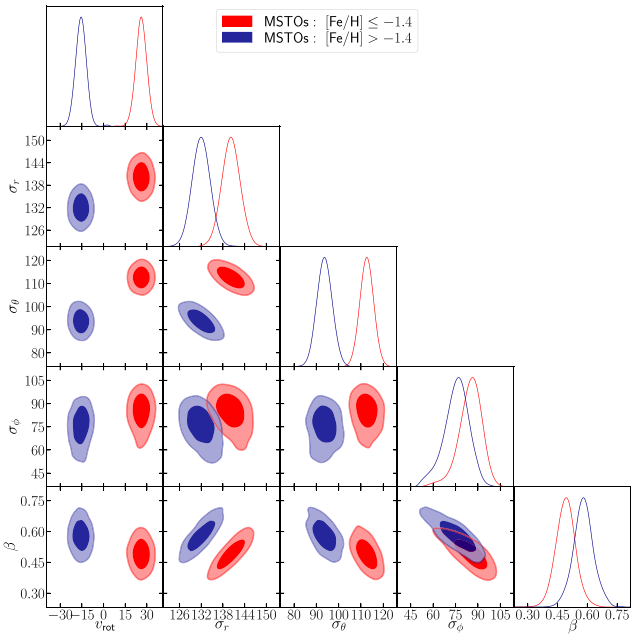

Figure 6. Kinematics of MSTOs. The contours show joint posterior probability distributions of the velocity moments and anisotropy to 1σ and 2σ credibility intervals and the histograms show one-dimensional marginalized posterior distribution. The blue and red colours show posteriori for the comparatively metal-rich ([Fe/H] > -1.4) and metal-poor ([Fe/H] ≤ -1.4) sub-sample of the MSTOs, respectively.

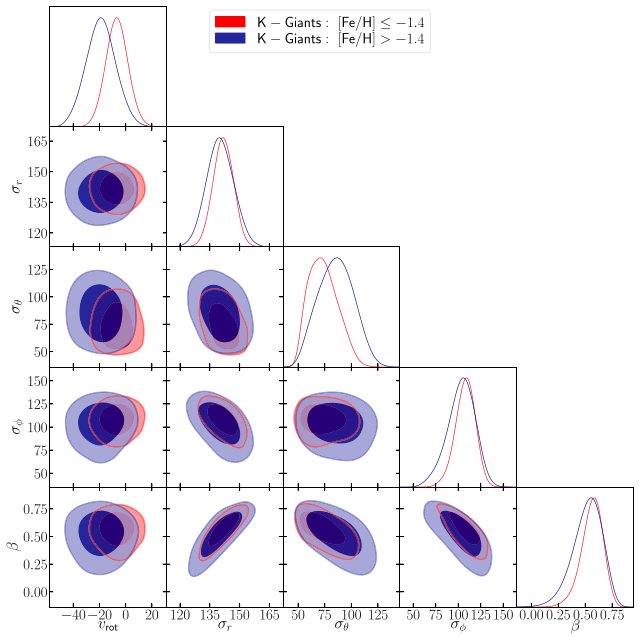

Figure 7. Kinematics of KGs. The contours show joint posterior probability distributions of the velocity moments and anisotropy to 1σ and 2σ credibility intervals and the histograms show one-dimensional marginalized posterior distribution. The blue and red colours show posteriori for the comparatively metal-rich ([Fe/H] > -1.4) and metal-poor ([Fe/H] ≤ -1.4) sub-sample of the KGs, respectively.

sample shows prograde motion ($-16 \pm 4\,{\rm km\,s^{-1}}$) while the metal-poor sample shows retrograde motion (26 ± 4 km s^{-1}). The mean difference between their $v_{\rm rot}$ is roughly 40 km s^{-1}. We also find that the $\sigma_{\rm r}$ and σ_θ of the two sub-samples of MSTOs are quite distinct, whereas the distinction is less clear for σ_ϕ. Similarly, there is also a small shift in the measured velocity anisotropies of the metal-rich ($\beta = 0.58^{+0.06}_{-0.05}$) and metal-poor ($\beta = 0.53 \pm 0.05$) sub-samples, i.e. the MSTOs are clearly radially biased. In the case of the KGs (Fig. 7), the distinction is less clear in the $v_{\rm rot}$ parameter and the velocity dispersions show almost no metallicity bias. While the metal-rich KGs do show significant prograde motion ($v_{\rm rot} = -20 \pm 10$ km s^{-1}), the metal-poor counterpart is consistent with no-rotation ($v_{\rm rot} = -7 \pm 8$ km s^{-1}) given the uncertainty. This could be due to the fact that the distances of KGs, which are essentially calibrated with the metallicity dependent colour-absolute magnitude relations obtained from clusters, are systematically biased leading to non-rotating metal-poor KGs. To investigate this we introduce arbitrary systematic shifts of 10 to 25 per cent in the KG distances and rerun the analysis for the discrepant metal-poor case. The experiment yields summary kinematics of $\beta = 0.55 \pm 0.1$ and $v_{\rm rot} = -6 \pm 9\,{\rm km\,s^{-1}}$. The estimated $v_{\rm rot}$ is again consistent with no-rotation. Recently, Deason et al. (2017) also investigated the kinematics of the KG sample obtained from Xue et al. (2014) and combined this with SDSS–*Gaia* proper motions. This analysis, and our conclusions presented above, concur that the metal-rich KG ensemble is in prograde motion. Also, though marginal, there is a rotation–metallicity bias in the KGs.

Here, we discuss the impact of priors and modelling biases on our final results. First, we assess the role of a choice of the power-law slope α of the radial distribution of stars, which enters into our calculation through equation (8). For this we vary α within a reasonable range $\in [2, 3]$; re-analysing all of the above data sets we find that varying α in this range results in negligible changes to the halo kinematics. An example of this can be seen in Fig. 8 where we show 1σ and 2σ regions of the joint probability distributions of the summary statistics (modified β and $v_{\rm rot}$) for SEGUE MSTOs for the choices of α. This is because the distance modulus distribution $p(\mu)$ is roughly $\propto s^{3-\alpha}$, which is roughly constant for $\alpha \in [2, 3]$. Similarly, we also re-analysed the metal-rich and metal-poor sub-samples of both the MSTOs and KGs for two additional choices of R_0/kpc: 8.0 and 8.5, which we find has no affect on our kinematic measurements. Also, we tested that our final results are robust for the choice of priors on $\sigma_{\rm r}$, σ_θ and σ_ϕ by ± 20 km s^{-1}, and v_l and v_b by ± 100 km s^{-1}.

In this work, the model parameters (velocity moments) are assumed to be constant functions of the galactocentric radius (r). This is mainly because we are exploring a small range in the galactocentric distance r/kpc $\in [4, 15]$. However, we would also like to investigate if there are any abrupt changes or gradients in the kinematics with distances. To study this, we further split our MSTO catalogue into r, and also $|z|$, bins divided at the median of the distributions (11 kpc and 5.3 kpc, respectively) and analyse each sub-sample separately. We could not do the same with KGs due

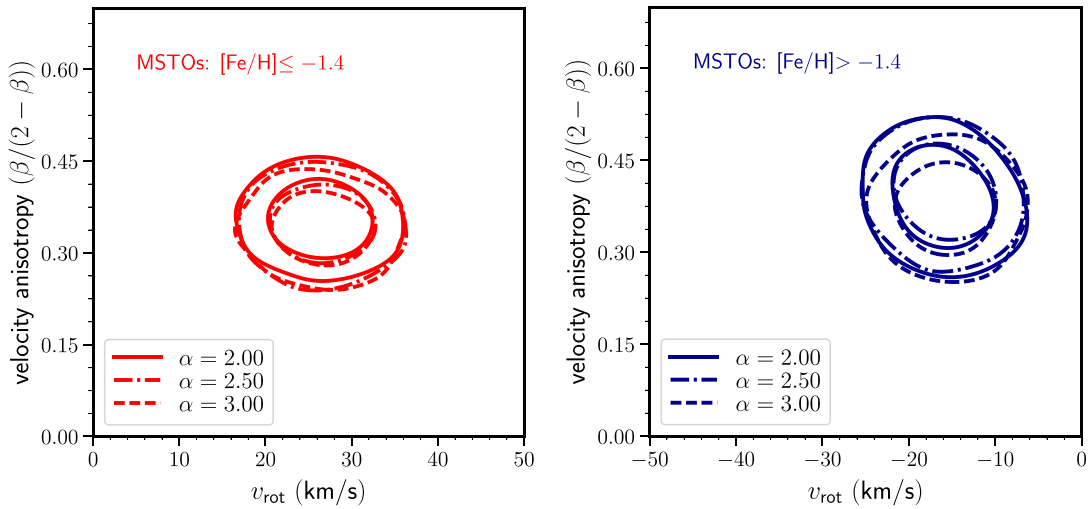

Figure 8. Effect of choice of power-law index α of the radial number density on the measurement of SEGUE MSTO kinematics.

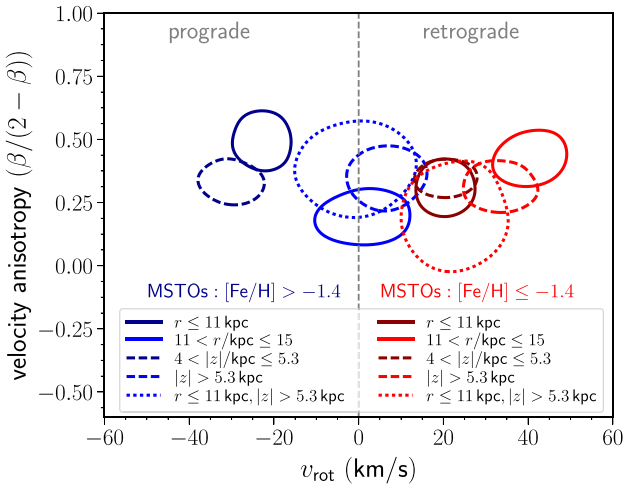

Figure 9. Kinematics of SEGUE MSTOs in radial (r) and height above the Galactic plane ($|z|$) bins. In cases where limits on r and $|z|$ are not explicitly provided, the limits are $r/{\rm kpc} \in [0, 15]$ or $|z|/{\rm kpc} > 4$.

to the small sample size. Joint probabilities of the summary kinematics (modified β and $v_{\rm rot}$) resulted from this study for both the metal-rich and metal-poor MSTO sub-samples are shown in Fig. 9 and the measurements (velocity moments, and also sample size) are presented in Table 1. We observe that both the metal-rich and metal-poor sub-samples do not show much deviation in velocity anisotropy but the shifts in $v_{\rm rot}$ are noticeable. In particular, inner sub-samples, i.e. $r/{\rm kpc} \leq 11$ and $|z|/{\rm kpc} \leq 5.3$ of both the metal-rich (shown in dark-blue solid and dashed lines, respectively) and metal-poor (shown in dark red solid and dashed lines, respectively) show leftward shifts, i.e. prograde shifts compared to the respective outer MSTO sub-sample (shown in light blue and light red). The observed leftward shift could be due to possible disc contaminants. However, systematic differences in the $v_{\rm rot}$ among the metal-rich and metal-poor sub-samples remain and retrograde motion of the metal-poor MSTO sub-samples persist. Albeit less significant, the offset in $v_{\rm rot}$ is still observed in the case where $r/{\rm kpc} \leq 11$ and $|z|/{\rm kpc} > 5.3$ (shown in dotted red and dotted blue). The large uncertainties here are because of the reduced sample size.

We provide a list of our final estimates of the model parameters in Table 1. Also, as a summary in Fig. 10, we compile the velocity anisotropy of the Galactic halo at different radii taken from various literature sources. Among the literatures labelled in the figure, it is worth noting that Smith et al. (2009a), Bond et al. (2010) and Cunningham et al. (2016) utilize the full phase-space motion of the stars whereas the remaining works (Kafle et al. 2012; Deason et al. 2013; King et al. 2015) only use the line-of-sight component of the velocity vector. The type of stars used in the referred works are also provided in the figure. The dashed line corresponds to an isotropic velocity distribution, i.e. $\beta = 0$. It is obviously clear that the β profile is not a monotonic function of the galactocentric radius. However, it can be stated that the inner stellar halo of the Galaxy is radial. Similarly, to put our results in context, in Fig. 11 we compare the $v_{\rm rot}$ and modified velocity anisotropy ($=\beta/(2-\beta)$) estimates for metal-rich and metal-poor sub-samples of three different types of

Table 1. Kinematics of the inner stellar halo of the MW.

Stellar population	Cases	Number of stars	$v_{\rm rot}$ (km s^{-1})	$\sigma_{\rm r}$ (km s^{-1})	σ_θ (km s^{-1})	σ_ϕ (km s^{-1})	β
MSTO and KG stars with $\lvert z\rvert/{\rm kpc} > 4$, and in different metallicity bins							
MSTOs	[Fe/H] ≤ -1.4, $r/{\rm kpc} \leq 15$	7426	26^{+4}_{-4}	141^{+3}_{-2}	109^{+4}_{-4}	82^{+8}_{-8}	$0.53^{+0.05}_{-0.05}$
MSTOs	[Fe/H] > -1.4, $r/{\rm kpc} \leq 15$	6693	-16^{+4}_{-4}	129^{+3}_{-2}	93^{+4}_{-4}	72^{+9}_{-9}	$0.58^{+0.06}_{-0.05}$
KGs	[Fe/H] ≤ -1.4, $r/{\rm kpc} \leq 17$	968	-7^{+8}_{-8}	142^{+5}_{-5}	70^{+10}_{-10}	110^{+10}_{-10}	$0.56^{+0.1}_{-0.1}$
KGs	[Fe/H] > -1.4, $r/{\rm kpc} \leq 17$	513	-20^{+10}_{-10}	140^{+7}_{-7}	90^{+20}_{-20}	100^{+20}_{-20}	$0.5^{+0.1}_{-0.1}$
Metal-poor ([Fe/H] ≤ -1.4) MSTOs in r and $\lvert z\rvert$ bins							
MSTOs	$\lvert z\rvert/{\rm kpc} > 4$, $r/{\rm kpc} \leq 11$	3495	20^{+5}_{-5}	139^{+6}_{-6}	108^{+5}_{-5}	90^{+10}_{-10}	$0.48^{+0.1}_{-0.09}$
MSTOs	$\lvert z\rvert/{\rm kpc} > 4$, $11 < r/{\rm kpc} \leq 15$	3930	40^{+6}_{-6}	142^{+4}_{-4}	110^{+10}_{-10}	60^{+8}_{-8}	$0.62^{+0.09}_{-0.08}$
MSTOs	$r/{\rm kpc} \leq 15$, $4 < \lvert z\rvert/{\rm kpc} < 5.3$	3677	21^{+5}_{-5}	136^{+3}_{-3}	103^{+4}_{-4}	84^{+9}_{-9}	$0.52^{+0.06}_{-0.06}$
MSTOs	$r/{\rm kpc} \leq 15$, $\lvert z\rvert/{\rm kpc} > 5.3$	3748	34^{+6}_{-6}	142^{+4}_{-4}	118^{+6}_{-6}	80^{+10}_{-10}	$0.49^{+0.08}_{-0.08}$
MSTOs	$\lvert z\rvert/{\rm kpc} > 5.3$, $r/{\rm kpc} \leq 11$	1362	23^{+8}_{-8}	140^{+10}_{-10}	121^{+9}_{-9}	100^{+20}_{-20}	$0.3^{+0.2}_{-0.2}$
Metal-rich ([Fe/H] > -1.4) MSTOs in r and $\lvert z\rvert$ bins							
MSTOs	$\lvert z\rvert/{\rm kpc} > 4$, $r/{\rm kpc} \leq 11$	2985	-23^{+5}_{-5}	135^{+5}_{-5}	84^{+6}_{-6}	70^{+10}_{-10}	$0.67^{+0.07}_{-0.07}$
MSTOs	$\lvert z\rvert/{\rm kpc} > 4$, $11 < r/{\rm kpc} \leq 15$	3705	1^{+7}_{-7}	122^{+4}_{-3}	114^{+6}_{-9}	70^{+10}_{-10}	$0.4^{+0.1}_{-0.1}$
MSTOs	$r/{\rm kpc} \leq 15$, $4 < \lvert z\rvert/{\rm kpc} < 5.3$	3472	-30^{+5}_{-5}	120^{+3}_{-3}	85^{+5}_{-5}	83^{+8}_{-8}	$0.51^{+0.07}_{-0.07}$
MSTOs	$r/{\rm kpc} \leq 15$, $\lvert z\rvert/{\rm kpc} > 5.3$	3218	6^{+6}_{-6}	133^{+4}_{-4}	107^{+7}_{-7}	70^{+10}_{-10}	$0.54^{+0.09}_{-0.09}$
MSTOs	$\lvert z\rvert/{\rm kpc} > 5.3$, $r/{\rm kpc} \leq 11$	1116	-1^{+9}_{-9}	134^{+9}_{-9}	104^{+10}_{-10}	70^{+10}_{-10}	$0.5^{+0.1}_{-0.1}$
MSTOs ($\lvert z\rvert/{\rm kpc} > 4$, $r/{\rm kpc} \leq 15$) with systematics							
MSTOs	$v_{\rm los} + 5$ km s^{-1}, [Fe/H] ≤ -1.4	7426	22^{+4}_{-4}	141^{+3}_{-3}	109^{+4}_{-4}	82^{+8}_{-8}	$0.53^{+0.05}_{-0.05}$
MSTOs	GALAXIA $M_{\rm r}$ calibration, [Fe/H] ≤ -1.4	5426	32^{+5}_{-5}	136^{+3}_{-3}	121^{+4}_{-4}	88^{+9}_{-9}	$0.39^{+0.07}_{-0.06}$
MSTOs	GALAXIA $M_{\rm r}$ calibration, [Fe/H] > -1.4	4879	-2^{+5}_{-5}	128^{+3}_{-3}	109^{+4}_{-4}	88^{+9}_{-9}	$0.39^{+0.08}_{-0.08}$

$\sigma_{\rm r}, \sigma_\theta, \sigma_\phi$ are the velocity dispersions in spherical coordinates, β is the velocity anisotropy parameter and $v_{\rm rot}$ is the mean azimuthal velocity measured in the galactocentric reference frame. A positive value for $v_{\rm rot}$ means retrograde motion, whereas a negative value means prograde motion i.e. rotating in the same direction the Galactic disc rotates.

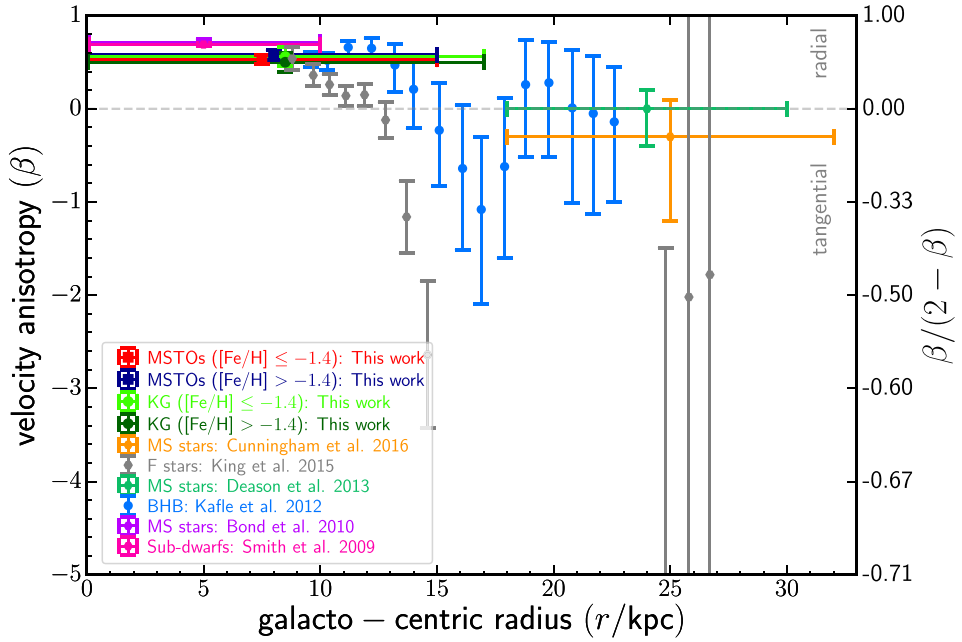

Figure 10. Velocity anisotropy profile of the MW stellar halo for different stellar populations taken from various literature sources as labelled in the figure. Red and dark-blue markers show our measurements for the metal-poor and metal-rich MSTOs, respectively, whereas bright-green and dark-green markers show our measurements for the metal-poor and metal-rich KGs, respectively.

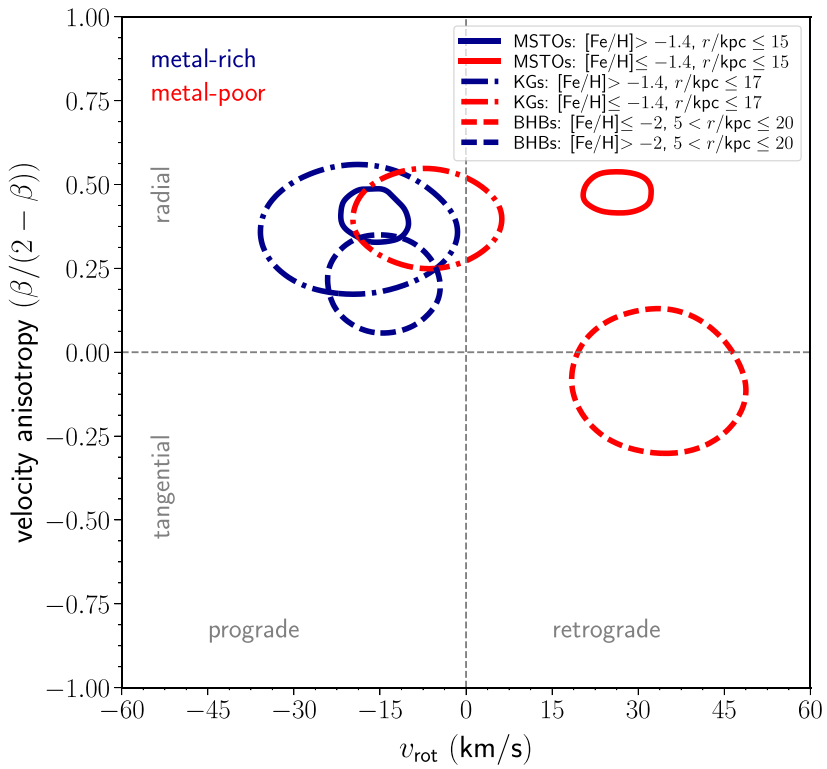

Figure 11. Joint distributions of the modified velocity anisotropy parameter (tangential = −1, radial = 1, isotropy = 0) and mean azimuthal velocity ($v_{\rm rot}$) for BHBs, MSTOs and KGs residing in the MW stellar halo.

stars namely, MSTOs, KGs and BHBs. The BHB results shown here are obtained from Kafle et al. (2013). Different stellar populations have different metallicity distributions that peak at different [Fe/H], e.g. BHBs are known to be a metal-poor population. Hence, exact division in the [Fe/H] distribution is not an issue, though note the radial coverage of BHBs is slightly different from that of MSTOs and KGs. There is a clear segregation in $v_{\rm rot}$ between metal-poor and metal-rich MSTOs and BHBs, which is less obvious in the case of

KGs. Though BHBs show a clear metallicity bias in anisotropy, it is smaller for MSTOs and negligible for KGs. This could be possibly because MSTOs, KGs and BHBs are different stellar populations and might be sampling different accretion events as well as the fractions of these stars sampled by SEGUE vary.

5.2 Discussion of the systematics

Finally, we would like to discuss the caveats/limitations of our work that could add systematics in our final results.

Assumption about constant velocity ellipsoid:

As discussed earlier, a key assumption in our work is that the velocity ellipsoids of the halo stars are aligned along the directions of the spherical polar coordinate frame of reference, centred at the Galactic Centre. While for the inner halo there is evidence supporting the alignment, it remains to be seen if the assumption holds beyond the solar neighbourhood. Similarly, because of the dwindling sample size we could only estimate the halo kinematics in coarse radial bins.

Effects of lack of proper motions and potential systematics in $v_{\rm los}$:

Importantly, one of the main limitation of our work is that we only use a line-of-sight ($v_{\rm los}$) component of the velocity vector for the stellar halo tracers. This is mainly because the variance or the uncertainty of the tangential velocities derived from the proper motions from the existing astrometric surveys are large. Moreover, proper motions of stars are known to have significant systematic errors due to frame-dragging and chromatic aberration, which demand a careful treatment (Fermani & Schönrich 2013b; Schönrich, Binney & Asplund 2012). We note in Fermani & Schönrich (2013b) that even the SEGUE $v_{\rm los}$ measurements, in particular for the metal-poor populations, could be systematically offset by $\sim$5 km s^{-1}. To investigate the effect of the above possible systematic on our final measurements, we add 5 km s^{-1} in the $v_{\rm los}$ for all the metal-poor MSTOs and rerun the MCMC. We find on the introduced systematic shift in the $v_{\rm los}$ makes no difference in the velocity dispersions of the metal-poor MSTO kinematics as we measure $\sigma_{\rm r} = 141 \pm 3$ km s^{-1}, $\sigma_\theta = 109 \pm 4$ km s^{-1}, $\sigma_\phi = 82 \pm 8$ km s^{-1} and $\beta = 0.53 \pm 0.05$. Moreover, we measure $v_{\rm rot} = 22^{+4}_{-4}$ km s^{-1}, which marginally agrees within the 1σ interval in the case of no added systematic (Table 1). But the median value of $v_{\rm rot}$ is found to decrease by 4 km s^{-1}, which is of the similar order (5 km s^{-1}) the $v_{\rm los}$ has been systematically offset.

Effects of radial binning:

In our likelihood analysis, we utilize the full error distribution of the distances. But occasionally we need to split our data into different spatial, i.e. r and z bins (e.g. in Fig. 9, or to select halo stars etc.) using the point estimates of the distances. Also, in Ivezić et al. (2008) we note that a disc–halo transition occurs roughly at 3 kpc, and to select the halo stars we use the $|z| > 4$ kpc cut. None the less, due to large distance uncertainties it is possible that the disc–halo separation may not be perfectly cleaned. As we discussed earlier, this could be a reason why we observe that the inner-most halo sample shows relatively more prograde motion compared to the sample in the outer bins (dark-blue/red contours are leftward shifted compared to the light-blue/red contours in Fig. 9). However, even in the outer bins, e.g. a case of $|z| > 5.3$ kpc, where we assume the halo samples are cleaner, the metallicity–kinematics bias persists.

Effects of potential systematics in Ivezić et al. (2008) relation:

We demonstrated in Section 4 that the $M_{\rm r}$ calibration shown in equation (3) and taken from Ivezić et al. (2008) underpredicts $M_{\rm r}$ for the GALAXIA MSTOs, on average by +0.37 mag. While testing the robustness of the Ivezic et al. relation is beyond the scope of this work, in light of the systematics we observe from GALAXIA, it is crucial to investigate its effect on our final results. For this we utilize the $M_{\rm r}$([Fe/H], $g_0 - i_0$) relation directly obtained from GALAXIA instead of the one adopted from Ivezić et al. (2008) to calculate distances for SEGUE MSTOs. The remaining prescription of the analysis are kept exactly the same as in the original case presented in Section 5.1. In the bottom two rows of Table 1, we provide the kinematics of the SEGUE MSTOs obtained from this exercise. We observe that both the metal-rich and metal-poor MSTO sample shows increased retrograde motion of $\sim$10 km s^{-1} in comparison with the original values for $v_{\rm rot}$. Note, even with the added systematic in the $M_{\rm r}$ calibration, we still observe a significant $v_{\rm rot}$–metallicity bias; the difference in $v_{\rm rot}$ of metal-rich and metal-poor sub-samples is $\sim$35 km s^{-1}. The velocity anisotropies have, however, decreased from 0.5 in the original cases to 0.39 for the current samples, still suggesting mildly radial orbits for the halo stars.

Effects of (sub)structures present in the Galactic halo:

It is evident from numerous recent observations that the Galactic halo contains a plethora of coherent stellar debris (substructures) (for review, see Helmi 2008; Grillmair & Carlin 2016). Similarly, as we discussed earlier, there are also pieces of evidence of the presence of kinematically coherent planar structures of the satellite galaxies in the halo (Ibata et al. 2013, 2015; Libeskind et al. 2015; Pawlowski et al. 2015). It remains to be seen that to what level the unrelaxed stars dispersed from the planar structures or belonging to distinct substructures contribute to the observed kinematic biases in the halo.

6 CONCLUSION

In this paper, we model the kinematics of the inner stellar halo ($r \lesssim 15$ kpc) of the MW galaxy to estimate the mean azimuthal velocity (streaming motion), velocity dispersion and anisotropy of the MSTO and KG stars. The stellar catalogues are constructed from the SEGUE survey (Yanny et al. 2009). In the following, we summarize our main findings.

(i) We find that the comparatively metal-rich sub-samples of all three stellar populations i.e. MSTO ([Fe/H] > -1.4), KG ([Fe/H] > -1.4) and BHB ([Fe/H] > -1.2) inhabiting the MW inner halo are in prograde motion $\sim$20 km s^{-1}, whereas the metal-poor sub-samples of MSTO and BHB are in a clear retrograde motion of $\sim$25 km s^{-1}. The streaming motion of the metal-poor KGs is also lagging compared to their comparatively metal-rich counterpart. However, this lag is significantly smaller than in the cases of the metal-poor MSTO and BHB samples, which are clearly in retrograde orbits.

(ii) We find that the comparatively metal-rich ([Fe/H] > -1.4) and metal-poor ([Fe/H] ≤ -1.4) sub-populations of halo MSTOs show distinct kinematic properties. Importantly, the halo rotation velocity for the sub-populations are offset by $\sim$40 km s^{-1}. This is also

in agreement with our earlier findings using the BHB stars (Kafle et al. 2013). Some differences in the kinematics of the comparatively metal-rich ([Fe/H] > -1.4) and metal-poor ([Fe/H] ≤ -1.4) KGs are also observed but the distinction is not clear. Irrespective of the absolute magnitude calibrations obtained from Ivezić et al. (2008) or derived from Sharma et al. (2011b, GALAXIA) to estimate the distances, we observe similar level of kinematic–metallicity bias in the MSTOs. But, we find that the offset in $v_{\rm rot}$ is less significant (20 km s^{-1}) when stricter cuts in distances (r and/or $|z|$) are used to cull the disc stars. This hints that the net prograde signal is due to disc contamination, particularly the one detected in the metal-rich MSTOs.

(iii) Both the MSTOs and KGs are on radial orbits (velocity anisotropy $\beta \simeq 0.5$), and also velocity anisotropy (β) does not show any significant metallicity dependence.

In the near future, this work can be extended in two ways. First, we can utilize the Large Sky Area Multi-Object Fibre Spectroscopic Telescope survey (LAMOST; Deng et al. 2012) that provides almost an order-of-magnitude more halo stars of different stellar types, e.g. A-type, turn-off, giant, etc. Second, we would immensely benefit from the parallax distances and proper motions of the inner halo stars that the second and subsequent data releases of *Gaia* will deliver. Even further down the line, the synergy between *Gaia* and a follow-up radial velocity campaign will produce yet more precise kinematic inference and allow for full phase-space modelling of the Galactic halo.

ACKNOWLEDGEMENTS

In the sport of cricket a googly is a type of delivery by a right-arm leg spin bowler that spins from off to leg in the opposite direction to a normal leg break spin. Funding credit: PRK is funded through Australian Research Council (ARC) grant DP140100395 and The University of Western Australia Research Collaboration Award PG12104401 and PG12105203.

Software credit: GETDIST (Lewis & Bridle 2002), IPYTHON (Pérez & Granger 2007), MATPLOTLIB (Hunter 2007), NUMPY (van der Walt, Colbert & Varoquaux 2011), PANDAS (McKinney 2012) and SCIPY (Jones et al. 2001).

Content credit: We like to thank the anonymous referee, and Pascal Elahi for their useful comments.

Funding for SDSS-III has been provided by the Alfred P. Sloan Foundation, the participating institutions, the National Science Foundation and the U.S. Department of Energy Office of Science. The SDSS-III web site is http://www.sdss3.org/.

REFERENCES

Akhter S., Da Costa G. S., Keller S. C., Schmidt B. P., 2012, ApJ, 756, 23
An J., Evans N. W., 2016, ApJ, 816, 35
Battaglia G. et al., 2005, MNRAS, 364, 433
Beers T. C. et al., 2012, ApJ, 746, 34
Bekki K., Chiba M., 2001, ApJ, 558, 666
Bell E. F. et al., 2008, ApJ, 680, 295
Bell E. F., Xue X. X., Rix H.-W., Ruhland C., Hogg D. W., 2010, AJ, 140, 1850
Bertelli G., Bressan A., Chiosi C., Fagotto F., Nasi E., 1994, A&AS, 106, 275
Bird S. A., Flynn C., 2015, MNRAS, 452, 2675
Bland-Hawthorn J., Gerhard O., 2016, ARA&A, 54, 529
Bond N. A. et al., 2010, ApJ, 716, 1
Bowden A., Evans N. W., Williams A. A., 2016, MNRAS, 460, 329
Brown A. G. A., Velázquez H. M., Aguilar L. A., 2005, MNRAS, 359, 1287
Carlberg R. G. et al., 1997, ApJ, 485, L13
Carollo D. et al., 2007, Nature, 450, 1020
Carollo D. et al., 2010, ApJ, 712, 692
Cunningham E. C. et al., 2016, ApJ, 820, 18
Das P., Binney J., 2016, MNRAS, 460, 1725
De Silva G. M. et al., 2015, MNRAS, 449, 2604
Deason A. J., Belokurov V., Evans N. W., 2011a, MNRAS, 411, 1480
Deason A. J., Belokurov V., Evans N. W., 2011b, MNRAS, 416, 2903
Deason A. J., Belokurov V., Evans N. W., McCarthy I. G., 2012, ApJ, 748, 2
Deason A. J., Van der Marel R. P., Guhathakurta P., Sohn S. T., Brown T. M., 2013, ApJ, 766, 24
Deason A. J., Belokurov V., Koposov S. E., Gomez F. A., Grand R. J., Marinacci F., Pakmor R., 2017, MNRAS, preprint (arXiv:1703.09230)
Deng L.-C. et al., 2012, Res. Astron. Astrophys., 12, 735
Diakogiannis F. I., Lewis G. F., Ibata R. A., 2014, MNRAS, 437, 3172
Diakogiannis F. I., Lewis G. F., Ibata R. A., Guglielmo M., Kafle P. R., Wilkinson M. I., Power C., 2017, MNRAS, 470, 2034
Duarte M., Mamon G. A., 2015, MNRAS, 453, 3848
Eadie G. M., Harris W. E., 2016, ApJ, 829, 108
Evans N. W., Wilkinson M. I., Perrett K. M., Bridges T. J., 2003, ApJ, 583, 752
Fermani F., Schönrich R., 2013a, MNRAS, 430, 1294
Fermani F., Schönrich R., 2013b, MNRAS, 432, 2402
Font A. S., McCarthy I. G., Crain R. A., Theuns T., Schaye J., Wiersma R. P. C., Dalla Vecchia C., 2011, MNRAS, 416, 2802
Frenk C. S., White S. D. M., 1980, MNRAS, 193, 295
Gibbons S. L. J., Belokurov V., Evans N. W., 2014, MNRAS, 445, 3788
Girardi L., Grebel E. K., Odenkirchen M., Chiosi C., 2004, A&A, 422, 205
Gorski K. M., Wandelt B. D., Hansen F. K., Hivon E., Banday A. J., 1999, preprint (arXiv:e-prints)
Górski K. M., Hivon E., Banday A. J., Wandelt B. D., Hansen F. K., Reinecke M., Bartelmann M., 2005, ApJ, 622, 759
Grillmair C. J., Carlin J. L., 2016, Tidal Streams in the Local Group and Beyond, 420, 87
Hattori K., Yoshii Y., Beers T. C., Carollo D., Lee Y. S., 2013, ApJ, 763, L17
Hattori K., Valluri M., Loebman S. R., Bell E. F., 2017, ApJ, 841, 91
Helmi A., 2008, A&A Rev., 15, 145
Hunter J. D., 2007, Comput. Sci. Eng., 9, 90
Ibata R. A. et al., 2013, Nature, 493, 62
Ibata R. A., Famaey B., Lewis G. F., Ibata N. G., Martin N., 2015, ApJ, 805, 67
Ivezić Ž. et al., 2008, ApJ, 684, 287
Johnson D. R. H., Soderblom D. R., 1987, AJ, 93, 864
Jones E., Oliphant T., Peterson P. et al., 2001, SciPy: Open source scientific tools for Python, Available at: http://www.scipy.org/
Kafle P. R., Sharma S., Lewis G. F., Bland-Hawthorn J., 2012, ApJ, 761, 98
Kafle P. R., Sharma S., Lewis G. F., Bland-Hawthorn J., 2013, MNRAS, 430, 2973
Kafle P. R., Sharma S., Lewis G. F., Bland-Hawthorn J., 2014, ApJ, 794, 59
King III C., Brown W. R., Geller M. J., Kenyon S. J., 2015, ApJ, 813, 89
Lee Y. S. et al., 2008, AJ, 136, 2022
Lewis A., Bridle S., 2002, Phys. Rev. D, 66, 103511
Libeskind N. I., Hoffman Y., Tully R. B., Courtois H. M., Pomarède D., Gottlöber S., Steinmetz M., 2015, MNRAS, 452, 1052
Loebman S. R. et al., 2017, ApJ, preprint (arXiv:1704.06264)
Łokas E. L., 2009, MNRAS, 394, L102
Lynden-Bell D., 2016, MNRAS, 458, 726
Majewski S. R., 1992, ApJS, 78, 87
Majewski S. R., 1993, ARA&A, 31, 575
Marigo P., Girardi L., Bressan A., Groenewegen M. A. T., Silva L., Granato G. L., 2008, A&A, 482, 883
Martell S. L. et al., 2017, MNRAS, 465, 3203
McCarthy I. G., Font A. S., Crain R. A., Deason A. J., Schaye J., Theuns T., 2012, MNRAS, 420, 2245

McKinney W., 2012, Python for Data Analysis: Data Wrangling with Pandas, NumPy, and IPython. O'Reilly Media, Inc.
Pawlowski M. S., McGaugh S. S., Jerjen H., 2015, MNRAS, 453, 1047
Pérez F., Granger B. E., 2007, Comput. Sci. Eng., 9, 21
Rashkov V., Pillepich A., Deason A. J., Madau P., Rockosi C. M., Guedes J., Mayer L., 2013, ApJ, 773, L32
Ratnatunga K. U., Freeman K. C., 1989, ApJ, 339, 126
Reid M. J., Brunthaler A., 2004, ApJ, 616, 872
Schönrich R., Binney J., Dehnen W., 2010, MNRAS, 403, 1829
Schönrich R., Asplund M., Casagrande L., 2011, MNRAS, 415, 3807
Schönrich R., Binney J., Asplund M., 2012, MNRAS, 420, 1281
Schönrich R., Asplund M., Casagrande L., 2014, ApJ, 786, 7
SDSS Collaboration et al., 2016, ApJS, preprint (arXiv:1608.02013)
Sesar B., Jurić M., Ivezić Ž., 2011, ApJ, 731, 4
Sharma S., Johnston K. V., Majewski S. R., Bullock J., Muñoz R. R., 2011a, ApJ, 728, 106
Sharma S., Bland-Hawthorn J., Johnston K. V., Binney J., 2011b, ApJ, 730, 3
Sharma S. et al., 2014, ApJ, 793, 51
Sharma S. et al., 2017, preprint (arXiv:170601629)
Sirko E. et al., 2004, AJ, 127, 914
Smith M. C. et al., 2009a, MNRAS, 399, 1223
Smith M. C., Wyn Evans N., An J. H., 2009b, ApJ, 698, 1110
Smolinski J. P. et al., 2011, AJ, 141, 89
Sommer-Larsen J., Flynn C., Christensen P. R., 1994, MNRAS, 271, 94
Tissera P. B., Beers T. C., Carollo D., Scannapieco C., 2014, MNRAS, 439, 3128
van der Walt S., Colbert S. C., Varoquaux G., 2011, Comput. Sci. Eng., 13, 2
Veljanoski J. et al., 2013, ApJ, 768, L33
Watkins L. L. et al., 2009, MNRAS, 398, 1757
Watkins L. L., Evans N. W., An J. H., 2010, MNRAS, 406, 264
Wojtak R., Łokas E. L., 2010, MNRAS, 408, 2442
Wojtak R., Gottlöber S., Klypin A., 2013, MNRAS, 434, 1576
Xue X. X. et al., 2008, ApJ, 684, 1143
Xue X.-X. et al., 2011, ApJ, 738, 79
Xue X.-X. et al., 2014, ApJ, 784, 170
Xue X.-X., Rix H.-W., Ma Z., Morrison H., Bovy J., Sesar B., Janesh W., 2015, ApJ, 809, 144
Yanny B. et al., 2009, AJ, 137, 4377
York D. G. et al., 2000, AJ, 120, 1579
Zolotov A., Willman B., Brooks A. M., Governato F., Brook C. B., Hogg D. W., Quinn T., Stinson G., 2009, ApJ, 702, 1058
Zuo W., Du C., Jing Y., Gu J., Newberg H. J., Wu Z., Ma J., Zhou X., 2017, ApJ, 841, 59

APPENDIX: TRANSFORMING PHASE-SPACE COORDINATES TO GALACTIC/ GALACTOCENTRIC COORDINATES

Here, we provide the transformation formulary to convert phase-space coordinates from the galactic (centred at the Sun) to the galactocentric (centred at the centre of the Galaxy) frame of reference, i.e.

$$(l, b, d_{\rm gc}, v_l, v_b, v_{\rm los}) \longrightarrow (r_{\rm GC}, \theta_{\rm GC}, \phi_{\rm GC}, v_{\rm r}, v_\theta, v_\phi). \tag{A1}$$

First, we assume a generic basis vector transformation matrix

$$\mathbf{T}(\theta, \phi) = \begin{bmatrix} \sin(\theta)\cos(\phi) & \sin(\theta)\sin(\phi) & \cos(\theta) \\ \cos(\theta)\cos(\phi) & \cos(\theta)\sin(\phi) & -\sin(\theta) \\ -\sin(\phi) & \cos(\phi) & 0 \end{bmatrix}. \tag{A2}$$

To transform from spherical galactic coordinates $(l, b, d_{\rm gc})$ to the Cartesian coordinates we use

$$\begin{bmatrix} x_{\rm gc} \\ y_{\rm gc} \\ z_{\rm gc} \end{bmatrix} = \mathbf{T}^{-1}(90^\circ - b, l) \begin{bmatrix} 0 \\ 0 \\ d_{\rm gc} \end{bmatrix}, \tag{A3}$$

where $d_{\rm gc}$ is a heliocentric distance to a star. Similarly, velocities in spherical galactic coordinates $(v_l, v_b, v_{\rm los})$ can be converted to Cartesian coordinates as follows

$$\begin{bmatrix} vx_{\rm gc} \\ vy_{\rm gc} \\ vz_{\rm gc} \end{bmatrix} = \mathbf{T}^{-1}(90^\circ - b, l) \begin{bmatrix} v_{\rm los} \\ -v_b \\ v_l \end{bmatrix}. \tag{A4}$$

Now, we linearly shift the galactic phase-space Cartesian coordinates to the centre of the Galaxy using

$$\begin{aligned} &\{x_{\rm GC}, y_{\rm GC}, z_{\rm GC}\} = \{x_{\rm gc} - R_0, y_{\rm gc}, z_{\rm gc}\} \\ &\{vx_{\rm GC}, vy_{\rm GC}, vz_{\rm GC}\} = \{vx_{\rm gc} + U_\odot, vy_{\rm gc} + V_\odot + v_{\rm LSR}, \\ &\quad vz_{\rm gc} + W_\odot\}, \end{aligned} \tag{A5}$$

where we are ignoring the height of the Sun from the plane of the galactic disc, which would otherwise introduce an additional term in $z_{\rm gc}$.

Finally, we can convert the galactocentric Cartesian to spherical coordinates as follows.

$$\begin{aligned} r_{\rm GC} &= \sqrt{x_{\rm GC}^2 + y_{\rm GC}^2 + z_{\rm GC}^2} \\ \theta_{\rm GC} &= \cos^{-1} z_{\rm GC}/r_{\rm GC} \\ \phi_{\rm GC} &= \tan^{-1} y_{\rm GC}/x_{\rm GC} \end{aligned} \tag{A6}$$

and

$$\begin{bmatrix} v_r \\ v_\theta \\ v_\phi \end{bmatrix} = \mathbf{T}(\theta_{\rm GC}, \phi_{\rm GC}) \begin{bmatrix} vx_{\rm GC} \\ vy_{\rm GC} \\ vz_{\rm GC} \end{bmatrix}. \tag{A7}$$

In case the heliocentric equatorial coordinates and/or proper motions are to be used, one could refer to Johnson & Soderblom (1987) and Brown et al. (2005) for the extra steps that need to be undertaken.

This paper has been typeset from a TEX/LATEX file prepared by the author.